

Investigation of Plasma Detachment From a Magnetic Nozzle in the Plume of the VX-200 Magnetoplasma Thruster

Christopher S. Olsen, Maxwell G. Ballenger, Mark D. Carter, Franklin R. Chang Díaz, Matthew Giambusso, Timothy W. Glover, Andrew V. Ilin, Jared P. Squire, Benjamin W. Longmier, Edgar A. Bering, III, and Paul A. Cloutier

Abstract—Understanding the physics involved in plasma detachment from magnetic nozzles is well theorized, but lacking in large scale experimental support. We have undertaken an experiment using the 150-m³ variable specific impulse magnetoplasma rocket test facility and VX-200 thruster seeking evidence that detachment occurs and an understanding of the physical processes involved. It was found that the plasma jet in this experiment does indeed detach from the applied magnetic nozzle (peak field ~ 2 T) in a two part process. The first part involves the ions beginning to deviate from the nozzle field 0.8-m downstream of the nozzle throat. This separation location is consistent with a loss of adiabaticity where the ratio of the ion Larmor radius to the magnetic field scale length ($r_{Li}|\nabla B|/B$) becomes of order unity and conservation of the magnetic moment breaks down. Downstream of this separation region, the dynamics of the unmagnetized ions and magnetized electrons, along with the ion momentum, affect the plume trajectory. The second part of the process involves the formation of plasma turbulence in the form of high-frequency electric fields. The ion and electron responses to these electric fields depend upon ion momentum, magnetic field line curvature, magnetic field strength, angle between the particle trajectories, and the effective momentum transfer time. In stronger magnetic field regions of the nozzle, the detached ion trajectories are affected such that the unmagnetized ions begin to flare radially outward. Further downstream as the magnetic field weakens, for higher ion momentum and along the edge of the plume, the fluctuating electric field enables anomalous cross-field electron transport to become more dominant. This cross-field transport occurs until the electric fields dissipate ~ 2 -m downstream of the nozzle throat and the ion trajectories become ballistic. This transition to ballistic flow correlates well with the sub-to-super Alfvénic flow transition (β_k). There was no significant change observed to the applied magnetic field.

Index Terms—Argon, electromagnetic propagation in plasma media, magnetic field measurement, magnetohydrodynamics, magnetometers, physics, plasma applications, plasma engines, plasma measurements, plasma waves.

NOMENCLATURE

ICH	Ion cyclotron heating.
$\Omega_{c,e,i}$	Generic, electron, ion cyclotron frequency.
$\beta_{k,th}$	Kinetic, thermal beta.
B	Magnetic flux density [G].
D	Diffusion coefficient [m ² /s].
μ	Mobility [m ² /V/s].
ν	Collision frequency [Hz].
S, L	External ionization sources/losses [ions/s/m ²].
u, v_i	Ion velocity [m/s].
η	Plasma resistivity [ohm].
u_{de}	Drift velocity of electrons relative to ions [m/s].
τ_{eff}	Effective momentum transfer time [s].
r_{edge}	Projected magnetic plasma boundary [m].
V	Test particle velocity [m/s].
u_{\perp}	Cross-field electron velocity [m/s].
u_E	$E \times B$ drift velocity [m/s].
u_D	Diamagnetic drift velocity [m/s].
$\phi(x)$	Error function.
$\psi(x)$	First derivative of error function.
R_c	Radius of curvature [m].
Γ_{iz}	Axial ion flux [ions/s].
Φ_B	Axial magnetic flux [Wb].
J_{iz}	Axial current density [A/m ²].
f_i	Ion flux plume fraction.
f_{Φ}	Magnetic flux plume fraction.
r_L	Larmor radius [m].
E	Electric field [V/m].
q	Elementary charge [C].
E_i	Ion energy [eV].
ρ	Mass density [kg/m ³].
f_{LH}	Lower hybrid frequency [Hz].
$m_{e,i}$	Electron, ion mass [kg].
n_e	Electron density [m ⁻³].
T_e	Electron temperature [eV].
k_B	Boltzmann constant [erg/eV].
ϵ_0	Permittivity of free space [F/C].
$\ln \Lambda$	Coulomb logarithm.
θ	Pitch, divergence angle [°].

Manuscript received November 21, 2013; revised January 28, 2014 and March 25, 2014; accepted April 22, 2014. Date of publication May 30, 2014; date of current version January 6, 2015.

C. S. Olsen, M. G. Ballenger, M. D. Carter, F. R. C. Díaz, M. Giambusso, T. W. Glover, A. V. Ilin, and J. P. Squire are with Ad Astra Rocket Company, Webster, TX 77598 USA (e-mail: chris.olsen@adastrarocket.com; ballengerm@gmail.com; mark.carter@adastrarocket.com; info@adastrarocket.com; matthew.giambusso@adastrarocket.com; tim.glover@adastrarocket.com; andrew.ilin@adastrarocket.com; jared.squire@adastrarocket.com).

B. W. Longmier is with the Department of Aerospace Engineering, University of Michigan, Ann Arbor, MI 48109 USA (e-mail: longmier@umich.edu).

E. A. Bering, III is with the Department of Physics and Department of Electronics and Communications, University of Houston, Houston, TX 77204 USA (e-mail: eabering@uh.edu).

P. A. Cloutier is with the Department of Physics and Astronomy, Rice University, Houston, TX 77005 USA (e-mail: pac@rice.edu).

Color versions of one or more of the figures in this paper are available online at <http://ieeexplore.ieee.org>.

Digital Object Identifier 10.1109/TPS.2014.2321257

I. INTRODUCTION

PLASMA flowing through magnetic nozzles has been observed in many natural systems and is used in a variety of terrestrial applications ranging from plasma processing to electric propulsion [1], [2]. Similar to de Laval nozzles that convert random thermal motion into directed flow, magnetic nozzles are used to redirect the motion and momentum of the plasma flowing through the nozzle. To this end, a magnetic nozzle can be used to improve thrust efficiency and provide a means of controlling the plume geometry and plasma energy distribution functions. One issue facing the implementation of magnetic nozzles is the tendency of the plasma to remain magnetized or otherwise tied to the magnetic field lines forming the nozzle. Many theories have been proposed to address the physics of the plasma detachment process from magnetic nozzles that range from collisional resistive diffusion [3] to collisionless magnetohydrodynamic (MHD) field line stretching [4], [5], loss of adiabaticity [6], [7], and electron inertia [8], [9]. Despite the many theories attempting to explain this process, there has been an overall dearth of quality experimental data to fully support any one mechanism, and as a result knowledge of the physics of magnetic nozzles remains limited.

One device that is ideally suited to study the processes involved in magnetic nozzle plasma detachment is the variable specific impulse magnetoplasma rocket (VASIMR) VX-200 laboratory device [10]. A dipole-expanding magnetic nozzle is inherent to the design and the ion cyclotron resonance process in the second stage of the plasma rocket allows control of the ion energy, thus permitting the investigation into momentum-dependent detachment processes. Other main benefits of using this device are that it is situated within a 150-m³ vacuum facility where the plume is able to expand for several meters before terminating on any material surface, the pumping rate is sufficient to keep background neutral pressures low enough to minimize charge-exchange processes, and ramping to full power plasma operation within 100 ms is routine. An extensive experiment campaign where detailed mapping of the plasma plume in a volume extending more than 2-m downstream of the exhaust exit has been completed using the VASIMR VX-200 device operating at two power levels; 30 ± 0.4 and 100 ± 2 kW corresponding to the first stage helicon discharge alone and both stages together, respectively [2]. Data were taken during the early portions of the discharge, while background pressure remained below 2×10^{-4} torr. A variety of traditional plasma diagnostics were used to gather plume data. The plume mapping was performed by repositioning each of the diagnostics using a 2-axis step-motor driven translation stage with submillimeter resolution. The spatially dependent plume data were then analyzed to verify if separation of the plasma from the applied magnetic field had occurred and which of the leading detachment theories were most consistent with the data. This paper shall attempt to summarize the highlights of this experiment and provide new key insights into the physics of energized plasma flowing through an axial magnetic nozzle.

The rest of this paper is organized as follows. Section II describes the key components of the experiment, such as

the plasma source, environmental conditions, and plasma diagnostics showing that the setup is legitimate and the data taken is of high quality. Section III discusses the results of the data characterizing the behavior of the plume flowing in the conditions listed in Section II. Section IV concludes this paper with some of the general outcomes of the work, while proposing some future experiments and applications of magnetic nozzles.

II. EXPERIMENTAL SETUP

A laboratory experiment set on adequately measuring and quantifying the physics involved in the final stages of plasma flowing through a magnetic nozzle, the separation of the magnetized plasma from the field lines that form the nozzle, should have to meet a number of specific required conditions [1], [11]. The first of which is that the system be large enough for the detachment process to occur and that it have ample volume for the plume to expand unimpeded before neutralizing on the walls of the chamber. The second requirement is to have sufficiently low-vacuum conditions so as to minimize plasma to neutral interactions (e.g., particle sources and losses due to impact ionization or charge-exchange interactions), which will alter unimpeded fluxes and potentially mask the underlying physics. A third requirement involves exploring over an adequate scale length for a magnetic nozzle where the magnetic field strengths extend a few orders of magnitude so as to test over a wide range of potential physical processes. Finally, the experiment should be capable of measuring the relevant plasma properties across the scale length of the system enough to characterize the detachment process. The following sections will address that each of these requirements were met during our experiment. We begin with an overview of the plasma source and magnetic nozzle followed by descriptions of the vacuum facility used to create the proper conditions and plasma diagnostics needed to measure the plasma.

A. VASIMR VX-200 Engine

The VASIMR engine is a high-power electric propulsion system capable of varying the thrust and specific impulse, while operating at a fixed input power. This form of constant power throttling makes the VASIMR engine an attractive option for a wide range of prospective space missions. The main components of a VASIMR engine are the engine core, propellant source, magnet, and RF generators and are shown in Fig. 1. A key benefit in using the VASIMR engine to study magnetic nozzles is the magnetic field inherent to the design. The properly shaped field profile enables radio frequency (RF) wave transport and forms a dipole (far field) expanding nozzle. Plasma is generated by a 6.78-MHz high-power helicon [11]–[17], which serves as the first stage of the engine core. The second stage, known as ion cyclotron heating (ICH), energizes the ions by launching left-hand polarized slow mode waves from the high-field side of ion resonance [18]–[20]. This RF wave coupling mechanism requires that the plasma be fully magnetized and enables control of the ion velocity exiting the thruster.

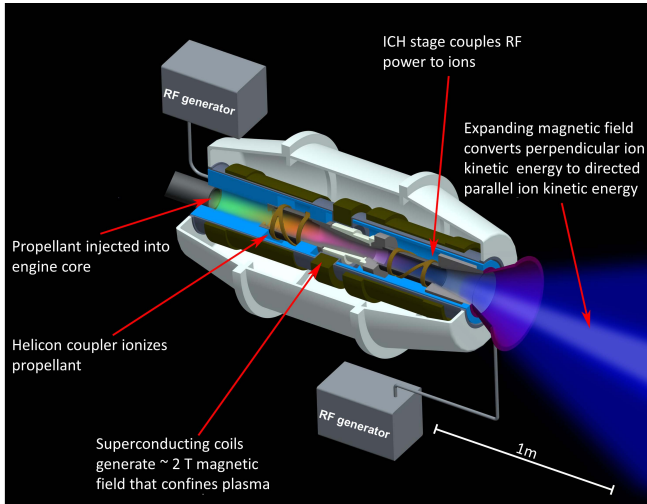


Fig. 1. Conceptual schematic of the VASIMR engine.

The VX-200 (VASIMR experimental—200 kW) device is a laboratory prototype operating from 2009 to 2012 demonstrating high-power densities (6 MW/m^2 across the exit area), specific impulse ranging between 2000 and 5000 s, and thrust up to 6 N. The magnetic field is generated by a cryogen-free, first generation (Nb-Ti) superconducting magnet encased in a well-insulated cryostat surrounding the engine core. It features a lightweight design and was fabricated by Scientific Magnetics of Oxford England, and produces a peak magnetic field strength of 2 T. The RF power is generated from two high-efficiency solid-state generators (combined conversion efficiency of 95% dc to RF) manufactured by Nautel Limited of Canada, and are independently controlled [21]. Impedance matching circuits are used to couple up to 98% of the RF power into the plasma. The RF generators are controlled using an in-house developed Field Programmable Gate Array circuit that provides precise synchronization between the units. Argon propellant is regulated through an injector plate into the first stage using a Moog propellant manifold. The manifold contains a proportional flow control valve, Taber industries low-pressure transducer, and a 0.041" diameter orifice flow controller. Choked flow enables mass flow rates up to 5000 sccm ($\sim 150 \text{ mg/s}$), which are verified using an in-line calibrated, NIST traceable, MKS-179 thermal mass flow controller. While the magnetic field is consistently active, timing of the gas flow, RF power, and plasma diagnostic are performed using a fiber optic triggering system synchronizing each system to within 6 ms from receiving the command.

B. Vacuum Facility

The experiment was carried out in a stainless steel vacuum chamber that is 4.3 m in diameter and 10-m long with a volume of 150 m^3 (including the end caps) located at the Ad Astra Rocket Company's Houston facility (Fig. 2). One end opens fully for complete access to the inner diameter of the chamber. The chamber is partitioned into two regions: 1) a rocket region and 2) a plume region. An anodized aluminum framed wall with Lexan paneling serves as the

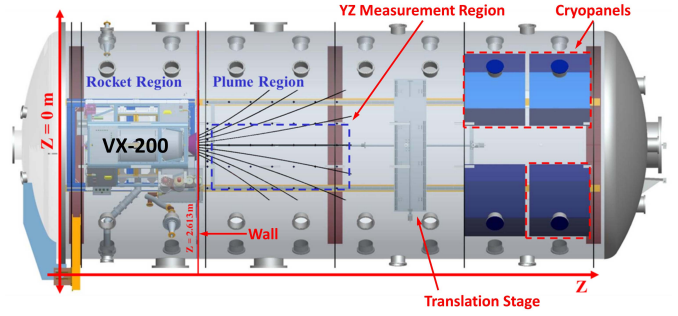


Fig. 2. Semitransparent schematic of the 10-m long \times 4.3-m diameter vacuum chamber and the VX-200 engine. Also shown are the translation stage, cryopumps, and locations of the measurement region and vacuum partition. All axial coordinates reference the end flange of the chamber.

partition, which is located at 2.613 m (nozzle throat is at $\sim 2.08 \text{ m}$) with $Z = 0 \text{ m}$ defined at the chamber door flange. The VX-200 engine is installed in the forward section of the chamber where a separate cryopump is used to maintain a lower pressure during firings so as to prevent arcing and glow discharges from forming near high-voltage RF components. The majority of the VX-200 components are located within the vacuum chamber with only the RF generators, magnet power supplies, and magnet cryocoolers maintained at atmospheric pressure. The plume region contains four CVI Torr-Master 1200i cryopumps, although for this experiment only three were used for a cumulative argon pumping speed of $175\,000 \text{ L/s}$ and an ultimate pressure of $\sim 1 \times 10^{-8} \text{ torr}$. The normal baseline pressure in between firings is $\sim 5 \times 10^{-8} \text{ torr}$ and rises as high as $2 \times 10^{-4} \text{ torr}$ argon after 1 s of plasma operation. Pressures in the plume region are measured using three separate hot cathode ion gauges.

C. Diagnostics and Translation Stage

To adequately measure many of the plasma properties relevant for characterizing the physics of plasma detachment from magnetic nozzles (e.g., plasma density, magnetic field strength, ion velocity, etc.), a wide variety of plasma diagnostics should be used over the spatial range where detachment may be occurring. The diagnostic used in this paper are shown in Fig. 3. They are (from left to right): retarding potential analyzer (RPA), HF electric field probe (recessed), backup plasma momentum flux sensor (PMFS), primary PMFS, 3-axis magnetometer, guard-ring Langmuir probe, azimuthal flux probe, lower ion flux probe array, and upper ion flux probe array. Most of these plasma probes are situated with its primary sensor or collector along the horizontal YZ plane of the rocket/chamber. Descriptions of each of the diagnostics pertinent to this paper, including translation stage are detailed below.

1) *Langmuir Probes*: There were two separate implementations of single planar Langmuir probes mounted on the translation stage: 1) a variable bias guard-ring probe [22] and 2) fixed bias ion flux probes. A single collector guard-ring probe was used to collect full current (I)–voltage (V) characteristics of the plasma whose bias ranged from -46 to 48 VDC . This particular probe was not RF compensated, but it

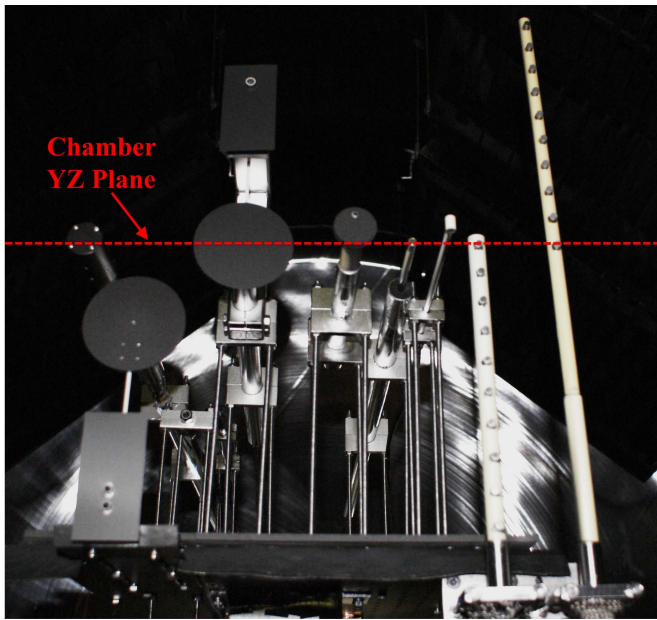


Fig. 3. Image of plasma diagnostics mounted on the translation stage.

has been characterized [23] under similar RF conditions to this experiment and the uncertainty is propagated through the data. The collector is surrounded by a stainless steel guard-ring at a gap distance of 0.13 mm to minimize sheath expansion effects. A pair of ten-collector fixed bias Langmuir probe arrays, spaced orthogonally along an alumina tube (Fig. 3), were used to measure ion flux. These ion flux probes were biased at -20 VDC into the ion saturation regime, which was verified to be $3T_e$ more negative than the floating potential during each firing using the guard-ring I - V characteristics. The collectors for all of the Langmuir probes consisted of high-purity 0.64-cm diameter molybdenum machined into a terraced design [24]. The Debye length, λ_D , in the plasma is much smaller than all collector dimensions ($\lambda_D < 15 \mu\text{m}$) and orbit limited collection is not a concern.

2) *Plasma Momentum Flux Sensor*: The PMFS was used to measure the amount of force imparted to the thruster carried away within the plasma stream. This method of measuring force has been characterized elsewhere [25], [27] and is an inexpensive alternative to traditional inverted pendulum thrust stands comparing well using the P5 Hall thruster [28]. The PMFS consists of a 9-cm diameter pyrolytic graphite disc attached to a $0.1 \text{ cm} \times 0.1 \text{ cm} \times 10 \text{ cm}$ insulating alumina rod. The opposite end of this stiff shaft is mechanically attached to a $5.7 \text{ cm} \times 1.3 \text{ cm}$ titanium bar where four Czochralski pulled boron doped silicon strain gauges are fixed to the titanium and connected in a Wheatstone bridge configuration. The output voltage is directly proportional to the amount of force causing strain. A small graphite shield is used to shadow the titanium bar/strain gauge assembly from the flowing plasma. The sensor is calibrated using tension applied from a set of precision masses and has a resolution of 0.1 mN. The probe has a natural frequency of oscillations of ~ 40 Hz and at least 3–4 periods (~ 100 ms) were averaged at minimum during data analysis.

3) *Retarding Potential Analyzer*: An RPA was used to deduce information about the ion distribution function (e.g., the parallel ion energy and temperature). This instrument was designed and maintained by the University of Houston and featured a four double grid arrangement [19]. The grids consisted of 35.4-wires/cm nickel mesh and spaced 0.1 cm apart using alumina spacers. Plasma passes through a 1-cm diameter graphite aperture before encountering an attenuation grid, a primary electron suppressor, an ion discriminator or a sweep grid, and a secondary electron suppressor before terminating on a molybdenum collector. The attenuation grid reduces the plasma density to permit the primary electron suppressor to repel incoming electrons. A variable bias voltage on the ion discriminator repels ions with flow kinetic energies below this retarding electrostatic potential, while those above will reach the collector. A secondary electron suppressor removes downstream electrons formed from secondary effects (i.e., secondary electron emission). The ion exhaust velocity and temperature are deduced from the current-retarding potential data using least-squares fits of drifting Maxwellians, which are a common analytical method for spacecraft RPA data [29], [30]. This RPA was mounted at the end of a step-motor driven goniometer, which permitted up to 90° articulation of the RPA head and analysis of parallel to perpendicular ion pitch angles. It has been estimated that this RPA is able to resolve multiple component ion populations as well as multiply ionized species, appearing as a stepped I - V characteristic, and are analyzed by fitting a multicomponent distribution [16], [31].

4) *Magnetometer*: Magnetic field measurements were made using an F. W. Bell 7030 Gauss/Tesla Meter using a ZOF73-3208-30-T 3-axis Hall probe. The Hall sensor elements are arranged orthogonally at the end of a 20.3-cm long aluminum fixture. Each Hall sensor has a capable range of 0–30 kG, a resolution of 0.1 mG, and is accurate to within 2%. The sensors are temperature compensated correcting to approximately $-0.05\%/^\circ\text{C}$ of temperature change. The Hall probe itself was thermally protected from the plasma flow as it was mounted within a round capped alumina sleeve in addition to being shadowed by a 3.8-cm diameter graphite disk (Fig. 3). This instrument may be used to measure magnetic fields from dc up to 50 kHz. A malfunction on one of the axis during an earlier detachment experiment made it necessary to have the instrument recalibrated. The 3-axis probe, full cable assemblies, and electronics box were calibrated to the ISO/EIC 17025 standard, which is the most rigorous and legally traceable calibration standard offered for this instrument. The experiment was repeated at a slightly lower mass flow rate.

5) *High-Frequency Electric Field Probe*: Having adequate information on the electric field, particularly the oscillating electric field, is important when studying charged particle flows. Knowledge of the range of frequencies and magnitude of electric fields in the plasma is telling to particle transport and instabilities that may exist throughout the magnetic nozzle system. The probe used to measure the oscillating electric field was designed and fabricated by the Alfvén lab in Stockholm and have used this type of probe previously to measure high-frequency electric characteristics in a plasma gun [32], [33].

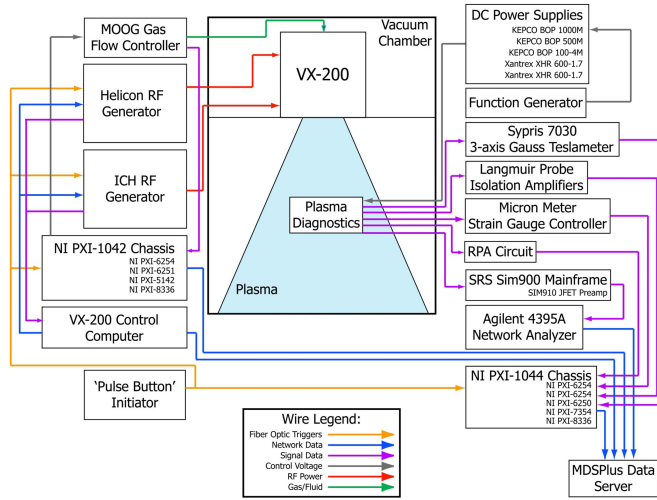


Fig. 4. Operational flowchart of a VX-200 firing.

It consists of a pair of 5-mm long by 0.3-mm diameter tungsten electrodes separated by 11.9 mm, along the Y axis, which are inserted into the plasma stream. Wire leads to the electrodes pass through alumina capillary tubing and multibore alumina tubing and terminate on a common transistor socket. The capillary tubing and alumina shaft are bonded using Torr-Seal, a thermally limited sealant, which prevented us from fully extending the axial range of this probe into the high-heat flux during ICH plasma. The probe was therefore recessed 33 cm behind the leading plane of the other diagnostics (Fig. 3). Nonetheless the probe was adequately exposed to the plasma stream.

The leads of the electrodes were passed through a SRS SIM910 JFET voltage preamp and fed into an Agilent 4395A Network/Spectrum/Vector analyzer, which measured the power spectrum between the electrodes. Spectra were taken every 500 ms from 0 to 10 MHz in steps of 12.5 kHz. The frequency dependent electric field is found using the peak-peak voltage backed out of the power spectrum divided by the separation distance of the electrodes. To reduce uncertainty ensemble smoothing was used to average several spectra taken during the same firing [34]. The probe, cabling, and electronics were *in situ* calibrated end to end over a 10-MHz frequency range by applying a 1 V_{pp} sinusoid across the electrodes using an Agilent 33220A waveform generator [1]. The corresponding obtain function was used to produce electric field spectra. Considering the probe operates in an RF environment, a vacuum (out of the plasma) spectrum was subtracted off the composite voltage spectrum. Mapping out the electric field spectra, as is shown in this paper, is important for understanding cross-field transport of electrons in the magnetic nozzle.

6) *Translation Stage:* Most of the plasma diagnostics used in this magnetic nozzle study were fixed on top of a movable 2-axis translation stage. Each axis of the 2 by 5-m translation stage was ball-screw driven using high-torque vacuum rated stepper motors from Lin Engineering. Microstepping features combined with the fine thread pitch of the ball-screws and low-backlash results in 0.1-mm position resolution. Positions are

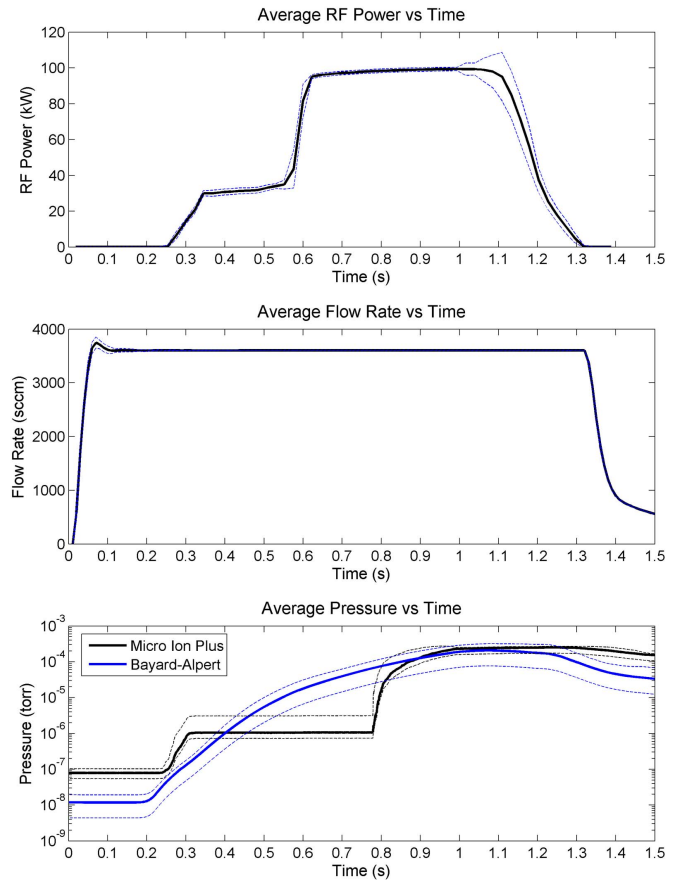


Fig. 5. Standard shot configuration including uncertainty bounds (dashed lines). Data analysis windows for the low- and high-power configurations were taken from 0.4–0.5 and 0.65–0.75 s, respectively. Top: average RF forward power profile. Middle: steady 3600-scm (~ 107 mg/s) argon flow. Bottom: exhaust region chamber pressure measured by separate hot cathode ion gauges.

calibrated using fixed inductive limit sensors referenced to the vacuum chamber door flange (Fig. 2). The movable portion of the translation stage is an elevated aluminum plate featuring regularly gridded tapped holes similar to an optical bench. The plasma diagnostics are further elevated above this aluminum plate to the chamber/nozzle centerline using threaded stainless steel rods. Exposed aluminum is covered by Grafoil sheets and pure graphite plate to minimize sputtering from the plasma stream.

D. Data Acquisition and Shot Parameters

An operational flowchart of a typical VX-200 firing showing synchronization of the gas, RF power, and Data Acquisition (DAQ) modules is shown in Fig. 4. A user depresses a physical pulse button initiating the firing sequence by launching a fiber optic pulse that is converted into a digital waveform and fed into the RF generators and National Instruments PXI chassis. The rising edge of this waveform causes the commanded preprogrammed gas flow and RF power profiles to run, while NI multifunction DAQ cards fill up sample buffers at rates of 40 and 100 kHz depending upon the specific diagnostic. For this experiment, a 2-s sample buffer is sufficient to collect plume data for a standard 100-kW power shot, as shown in Fig. 5. The solid lines are shot-averaged over

TABLE I

BASIC PLASMA PROPERTIES IN THE PLUME OF THE VX-200 DEVICE
MEASURED ON AXIS ($R = 0$ m) SPANNING THE MEASUREMENT
REGION ($Z = 2.8$ – 5.4 m) FOR BOTH OPERATING POWER LEVELS

On-Axis Parameter	Helicon (0.4 – 0.5 s)	Helicon + ICH (0.65 – 0.75 s)
n [m^{-3}]	$4.4 \times 10^{17} - 1.2 \times 10^{19}$	$5.3 \times 10^{17} - 8.4 \times 10^{18}$
T_e [eV]	1.3 – 2.2	2.1 – 6.2
T_i [eV]	6.6 – 10.2	27.6 – 37.1
B [G]	10 – 740	10 – 740
V_p [V]	2.8 – 6.1	7.6 – 15.8
v_i [km/s]	14 – 17	27 – 35
λ_{De} [μm]	3.2 – 13	6.4 – 15
r_{Le} [m]	$5.0 \times 10^{-3} - 2.7 \times 10^{-3}$	$8.0 \times 10^{-3} - 3.4 \times 10^{-3}$
r_{Li} [m]	0.02 – 2.1	0.05 – 3.9
v_A [km/s]	5.2 – 75	4.7 – 88
C_s [km/s]	5.8 – 7.0	10.9 – 13.2
r_{Li}/λ_{De}	$6.3 \times 10^3 - 1.6 \times 10^5$	$7.8 \times 10^3 - 2.6 \times 10^5$
Ω_e/ν_e	0.11 – 4.5	0.32 – 25

the entire experiment totaling more than 450 firings. Dashed lines represent 1σ uncertainty bounds to the averages. Despite the VX-200 laboratory device being capable of operating at 200-kW input power for short periods, due to the high rate of repetition it was decided to perform the experiment at reduced power so as not to overstress the device thus increasing the likelihood of finishing the tests without interruption.

For the purposes of data analysis, consistent data windows for each firing were from 0.4 to 0.5 s for the first stage and 0.65 to 0.75 s with the addition of the second stage. This corresponded to average power levels of 30 ± 0.4 and 100 ± 2 kW, respectively. The mass flow rate remained constant to within 0.5-sccm argon during these time spans. The exhaust region neutral pressure, as measured by separate ion gauges, was kept below 10^{-4} torr during these windows permitting charge–exchange mean free paths >12.6 and 1.3 m, respectively.

Since the aim of this experiment is to map out plasma properties in the plume, the translation stage was used to reposition the probes in between successive firings. The chosen approach was to perform radial position scans at fixed axial intervals with respect to the closest measurement location (~ 0.7 -m downstream the nozzle throat); a radial scan every $\Delta Z = 0.1$ m for the closest 1.0 m, $\Delta Z = 0.2$ m for next 0.4 m, and $\Delta Z = 0.4$ m for the final 0.8 m. The axial magnetic field strength decreases nearly two orders of magnitude over this span ($B_z \sim 740$ to 10 G). Each radial scan consisted of moving the translation stage from chamber centerline out to $R = 0.9$ m at intervals of $\Delta R = 0.05$ m in addition to allocating a firing to each plasma diagnostic when positioned along the nozzle axis creating higher spatial resolution near the center of the plume. A range of basic plasma properties measured along the magnetic nozzle centerline is presented in Table I.

III. EXPERIMENTAL RESULTS AND DISCUSSION

This is the first time a detailed large scale 2-D mapping of plume flow through an axial magnetic nozzle has been performed with the aim of studying the physics of plasma separation from the applied magnetic field. In determining

TABLE II

POWER LAW SCALING (Z^n) FITS TO THE EXPANDING ION, MOMENTUM,
AND MAGNETIC FLUXES DURING BOTH TIME WINDOWS AND
EXPANSION REGIONS

Parameter	n, Region 1 ($Z \approx 2.8 - 3.4$ m)		n, Region 2 ($Z \approx 3.4 - 5.4$ m)	
	Helicon	Helicon + ICH	Helicon	Helicon + ICH
Ion Flux	-10.1	-7.8	-5.5	-4.9
Momentum Flux	-7.7	-7.7	-5.0	-4.4
Magnetic Flux	-8.6	-8.6	-5.4	-5.4

plasma detachment, there are two challenges that need to be resolved: 1) obtain evidence that detachment has occurred and 2) verify if any currently accepted theories are applicable based on the behavior of the flow. For the first challenge, a simplified view of the problem of actually measuring plasma detachment is to see if the measured flow does not expand at the same rate at the magnetic field. An initial approach to quantify this notion is to compare the expansion of certain plasma parameters along the axis of the nozzle. Ion flux, momentum flux, magnetic flux, and parallel ion velocity data taken along the nozzle axis during both the helicon and helicon + ICH time windows are shown in Fig. 6.

There are several significant observations regarding the trends presented previously, the first of which is that there is virtually no difference in the measured magnetic field when the plasma is flowing when compared the applied magnetic field; the largest difference is 0.2 G. The second notable item is that there appears to be no additional acceleration or drag forces present as the parallel ion velocity is essentially flat indicating that the adiabatic conversion from perpendicular to parallel motion is complete. A final observation is that there are two regions of expansion during both time windows for the ion, momentum, and magnetic fluxes: 1) a fast expanding region over the first $\Delta Z \sim 0.6$ m and 2) a more gradual expansion region over the final $\Delta Z \sim 2$ m. It is useful to compare the rates of expansion for each of the fluxes. Exponential fits were initially used, but it was later determined that a power law scaling yielded superior coefficients of determination (>0.995). The best power law fits are displayed in Table II. These fits show, when comparing the falloff in concentration, that the plasma is not expanding with the magnetic field. Fits to the ion flux data show signs of divergent detachment (expanding faster than the magnetic field) during the low-energy helicon operation and convergent detachment during ICH when the ion energy increases by a factor of four. The ion flux data during the helicon phase may be indicative of radial ambipolar forces causing the ions to expand faster than the magnetic field and is overcome when the ion energy is increased. Power law fits to the momentum flux data from the PMFS, which is sensitive to both ions and neutrals, shows only convergent detachment when compared with the magnetic field during both modes of operation. The neutrals likely contribute a significant portion of the already weak signal of the PMFS during helicon operation and give the impression of convergent detachment. This proportional contribution is not the case during ICH as the much greater impact force of the ions dominates the much stronger signal.

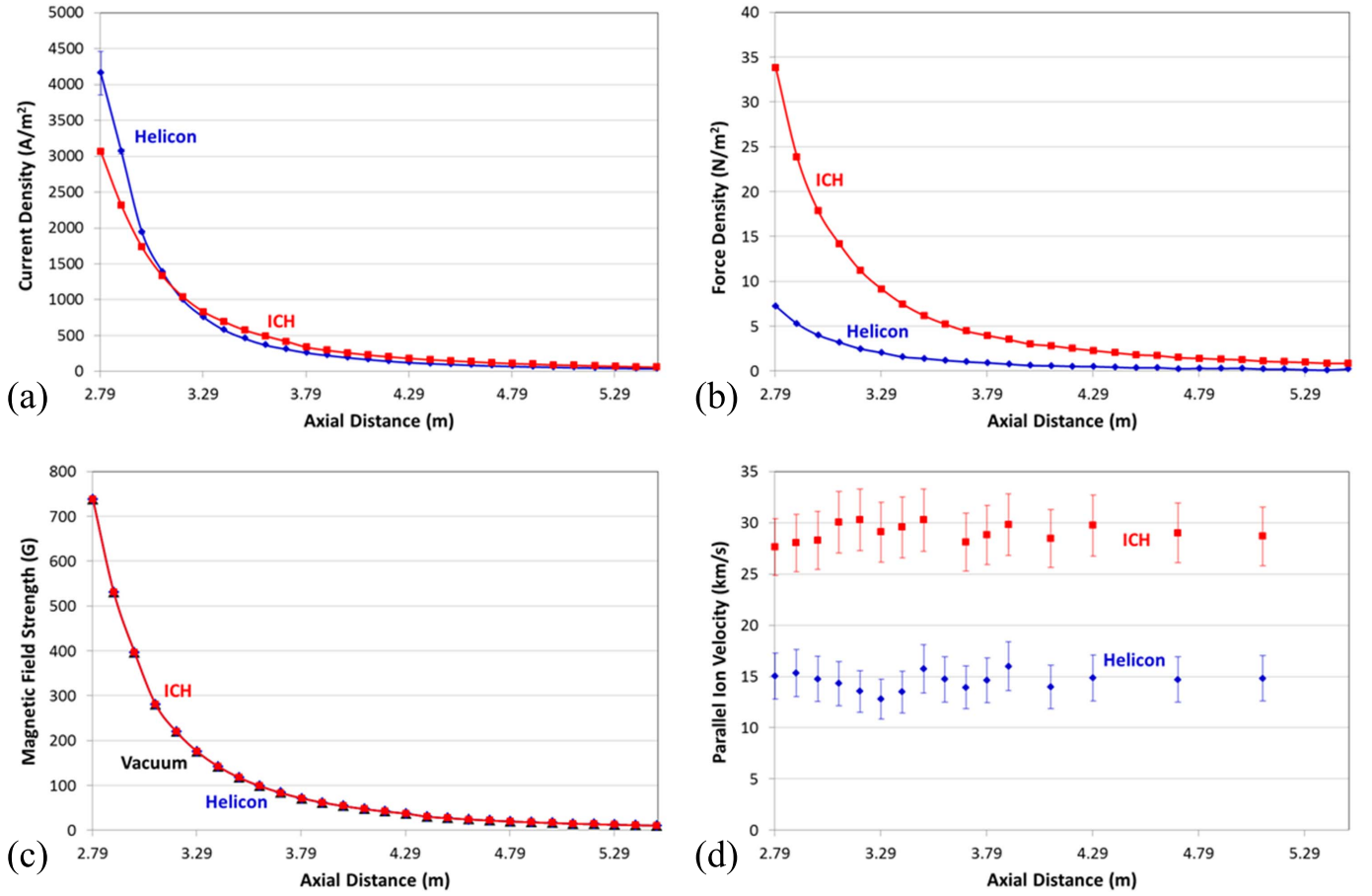


Fig. 6. Data taken along nozzle axis for the (a) ion flux, (b) momentum flux, (c) magnetic flux, and (d) parallel ion velocity during both helicon only (blue) and helicon + ICH (red) modes of operation. The applied (vacuum) magnetic field data is also shown (black). Error bars are displayed showing systematic uncertainty and were obtained through repeated firings.

Side-by-side comparisons of these data also including electron density/temperature and plasma potential (from guard-ring probe data) are shown in Fig. 7. Values are normalized to the most upstream datum point for each parameter. The same trends from the power law fits can be observed in Fig. 7 where neither the ion flux nor the momentum flux data are observed to follow the magnetic flux, which is an indication of detached flow

A. Ion Detachment

1) *Indications From Mapped Ion Flux and RPA Pitch Angle Scans*: The approach of comparing the axial expansions of flux may be expanded to the rest of the plume as a means of verifying detachment. This new method has been developed to compare spatially integrated ion flux and magnetic flux from measured data throughout the magnetic nozzle region of the exhaust plume and is shown in Fig. 8 [35]. The focus is turned to ion flux (rather than momentum flux) to better understand the behavior of ions in the magnetic nozzle. By comparing the change in radial position of the collective ion and magnetic flux, a detachment condition may be formed, which states that if the ratio of these quantities is unity the flow must be considered attached to the applied field. Deviation from unity is indicative of either convergent or divergent detachment.

The process begins with the continuity equation under the assumption that charge sources and losses are negligible and that the flow is in steady state

$$\frac{\partial \rho}{\partial t} + \nabla \cdot (\rho \bar{u}) = S - L \approx 0. \quad (1)$$

This form of the continuity equation is valid based on the steady mass flow rate shown in Fig. 5 and losses being minimized due to lower background pressures and interaction cross sections. The sources term is also presumed negligible based on verification from spectral data of a singly ionized plume, low-ion collision rate, and lack of additional external energy sources. The continuity equation permits the measurement of the plasma/magnetic flux expansion without worry of external influences. The ion flux probes are planar probes and restrict the comparison with only the axial components of ion and magnetic flux. The method continues by establishing a baseline integrated ion flux using data taken using a radial scan at the axial position closest to the nozzle ($Z \sim 2.79$ m). The ion flux is numerically integrated outward in radius from the peak of the plume to r_{edge} , a position determined from a geometric projection of the magnetic field from the inner wall of the engine core. The equations pertinent to

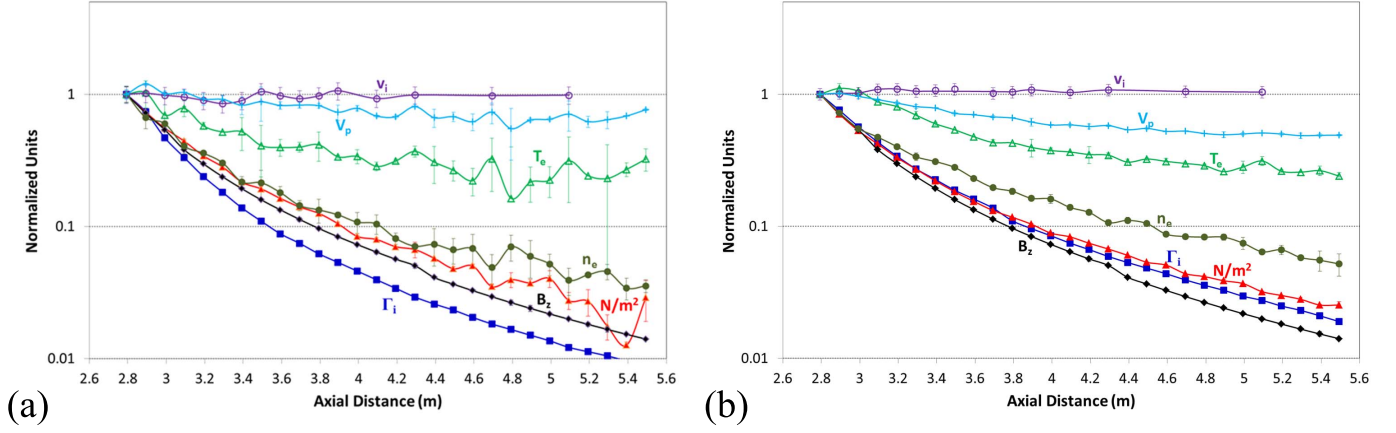


Fig. 7. Axial data comparison for multiple plume parameters during both (a) helicon and (b) helicon + ICH modes of operation. Data values are normalized to the closest measured datum point for each parameter.

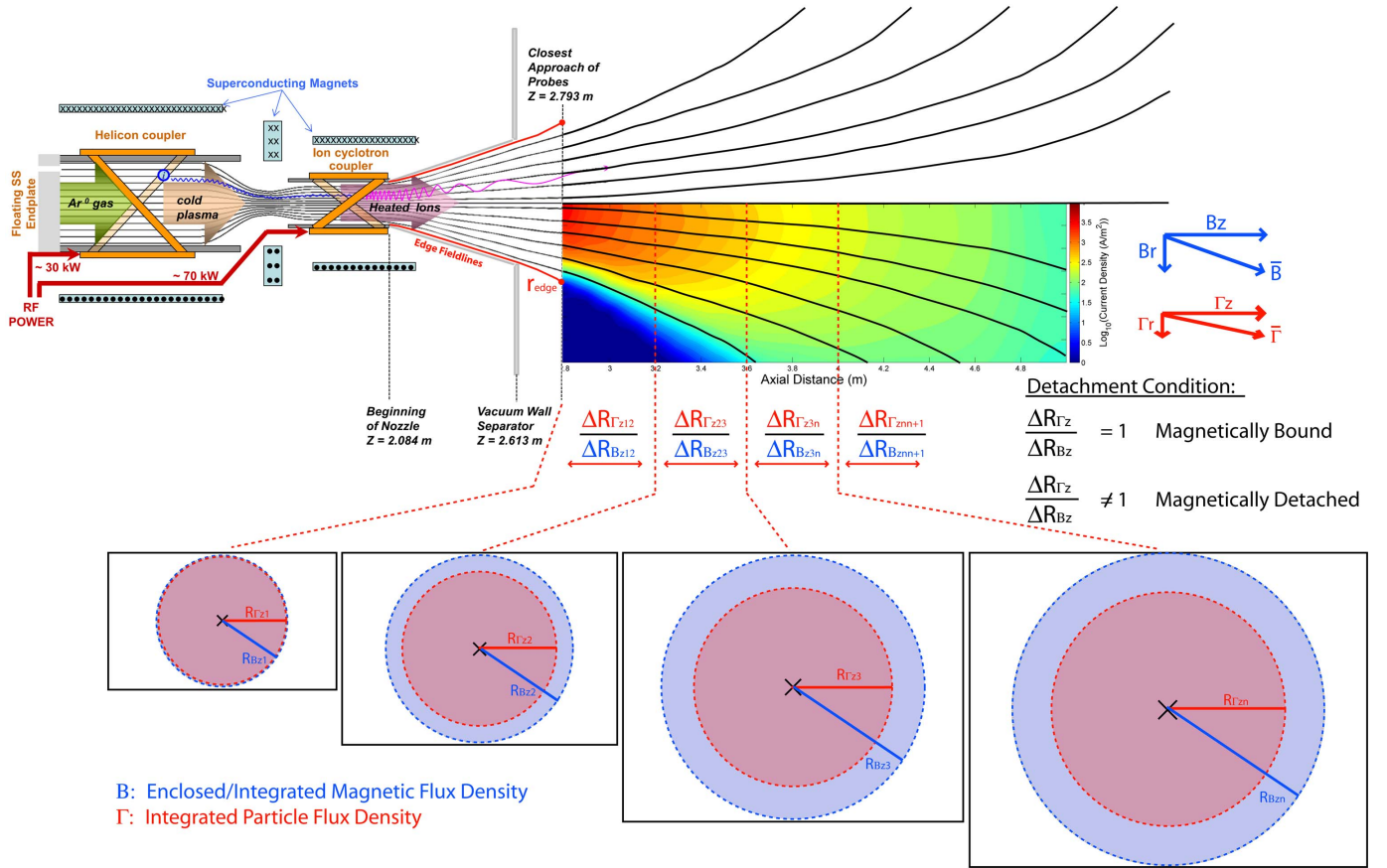


Fig. 8. Illustrating the method of spatially tracking lines of constant integrated ion flux and magnetic flux. Convergent detachment is shown (x-section insets) and appears as ion flux (pink) expanding slower than magnetic flux (blue).

this numerical integration, assuming azimuthal symmetry, are

$$\Gamma_{iz}(r) = 2\pi \int_0^r \frac{J_{iz}}{q} r dr \quad (2)$$

$$f_i(r) = \frac{\Gamma_{iz}(r)}{\Gamma_{0z}(r_{\text{edge}})} \quad (3)$$

$$\Phi_z(r) = 2\pi \int_0^r B_z r dr \quad (4)$$

$$f_\Phi(r) = \frac{\Phi_z(r)}{\Phi_{0z}(r_{fi})}. \quad (5)$$

Equations (2) and (3) describe the radial ion flux integration and ion plume fraction, f_i , which are used to map lines of constant integrated ion flux throughout the extent of the magnetic nozzle. Equations (4) and (5) are similar to the particle flux equations, except they detail the radial integration of magnetic flux and map lines of constant enclosed magnetic flux, that is, the expansion of the amount of magnetic flux enclosing the baseline ion flux. This set of operations was performed at each axial location where radial profile data were taken, and the fluxes were integrated outward until the flux

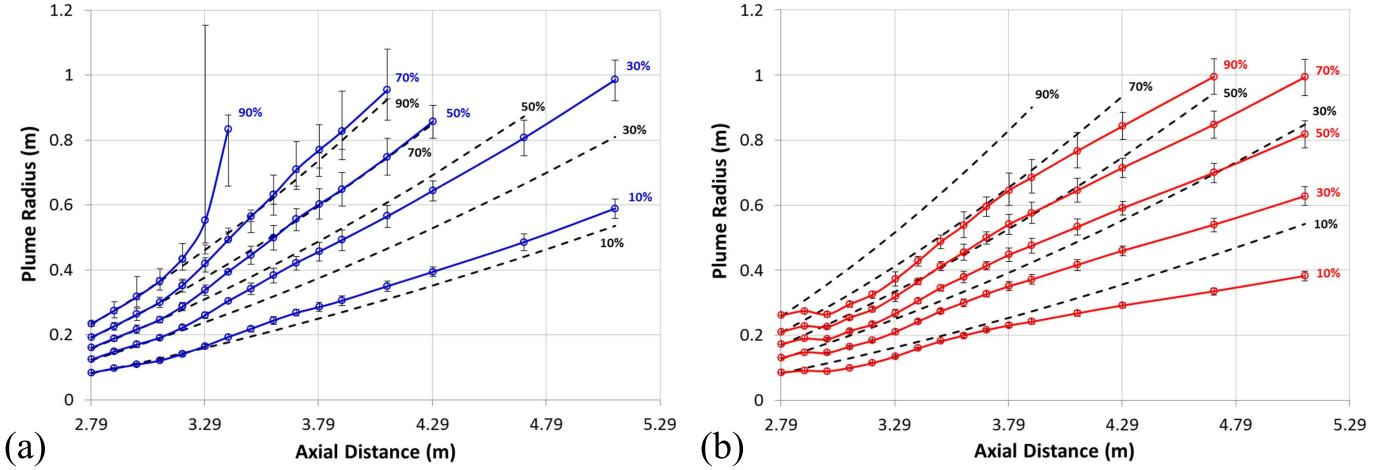


Fig. 9. Lines of constant integrated ion flux during the (a) helicon and (b) helicon + ICH phases of operation compared with lines of constant enclosed magnetic flux (black dashed). To avoid excessive clutter only odd plume fractions (by 10%) are displayed.

matched discrete values of the plume fraction (f_i , $f_\phi = 0.05$ to 0.9, in steps of 0.05). Results of these integrations are shown in Fig. 9. The data displayed along each of the trends are where the integration was able to measure the value of the ion plume fraction. Some of the plotted series have fewer points as a result of the integration failing to measure certain values of the ion plume fraction within the radial limits of the translation stage. Resultant error bars are displayed, having been computed and passed through the integration, assuming the maximum and minimum error of the baseline profile which propagates systematic uncertainty and errors introduced during interpolation. The large upper error bar during the helicon phase was a result of the numerical integration failing to measure the ion plume fraction and defaulting to the maximum radial position.

There are several notable trends to point out from the plotted integrations. First and foremost is that the measured ion flux deviates from the magnetic flux that originally encloses the plasma for all plume fractions. The difference between the helicon and helicon + ICH cases is not whether the ion flow separates from the applied magnetic field, but where the separation begins. The addition of energy to the ions via ion cyclotron resonance heating causes a doubling of parallel ion velocity ($4 \times E_i$) resulting in the separation from the magnetic field to occur at least ~ 0.4 m further upstream (judging from the inner 50% flux surfaces). The second observation is that these integrations agree with the axial data comparisons in that the helicon case shows divergent detachment, where the helicon + ICH is convergent. The detached ion flow for the helicon case may cross back over the magnetic field lines further outward and/or downstream as the magnetic field turns back on itself, but is inconclusive due to limitations of translation stage measurement range. Small radial variations, such as the apparent inward radial shift at $z = 2.9$ m, may be due to other experimental uncertainty, does not significantly affect the trends discussed in this paper.

Another aspect of these lines of constant ion flux is the trend of the lines themselves. Focusing on the helicon + ICH

case [Fig. 9(b)], one may divide the flow into separate regions based on the behavior of the flow: 1) a magnetized region; 2) a detached but expanding region; 3) a transition region; and 4) a ballistic/linear expansion region. The ions appear to follow the magnetic field for only a short distance ($\Delta Z \sim 0.1$ m) before deviating from the enclosed magnetic flux from $Z \approx 2.8$ to 2.9 m. Shortly after separating from the magnetic nozzle field the ions undergo a gradual expansion, radially outward, for approximately $\Delta Z \sim 0.6$ m between $Z \approx 2.9$ to 3.5 m. Although the ions have detached from the applied magnetic field, they are still subject to interparticle/wave forces, which are believed to influence this radial expansion. A transition region is seen as the trends begin to roll over beginning with the inner plume ($f_i = 10\%$) at $Z \sim 3.5$ m ending along the plume edge ($f_i = 90\%$) at $Z \sim 3.9$ m. Downstream of this transition region ($Z > 3.9$ m) the lines of constant ion flux expand linearly, exhibited by linear fits with excellent coefficients of determination (> 0.999), and the ion plume is therefore ballistic. Throughout these regions the interactions between the ions and magnetized electrons become important and shall be discussed further below. Further examination of the interparticle forces causing the downstream transition, or convergent bending, is beyond the scope of this paper and will be explored in the future.

An alternative method to compare the expansion rates of ion and magnetic fluxes for confirming detachment one may compare ion velocity vectors to magnetic field vectors through measurement of the pitch angle distribution. The distribution of ion velocity vectors is measured using an articulating RPA repositioned by a step motor driven goniometer to change the angle of the entrance grids with respect to the incoming plasma flow. An angular scan from $\theta = 0^\circ$ to 90° , at intervals of $\Delta\theta = \{5^\circ, 10^\circ, \text{ and } 20^\circ\}$, was performed at five radial locations between $R = 0$ to 0.4 m at an axial position of approximately 2-m downstream of the nozzle throat. An angle of $\theta = 0^\circ$ corresponds to the RPA oriented parallel to the nozzle axis. Contour plots of the ion velocity distribution function from these data as a function of radial versus axial

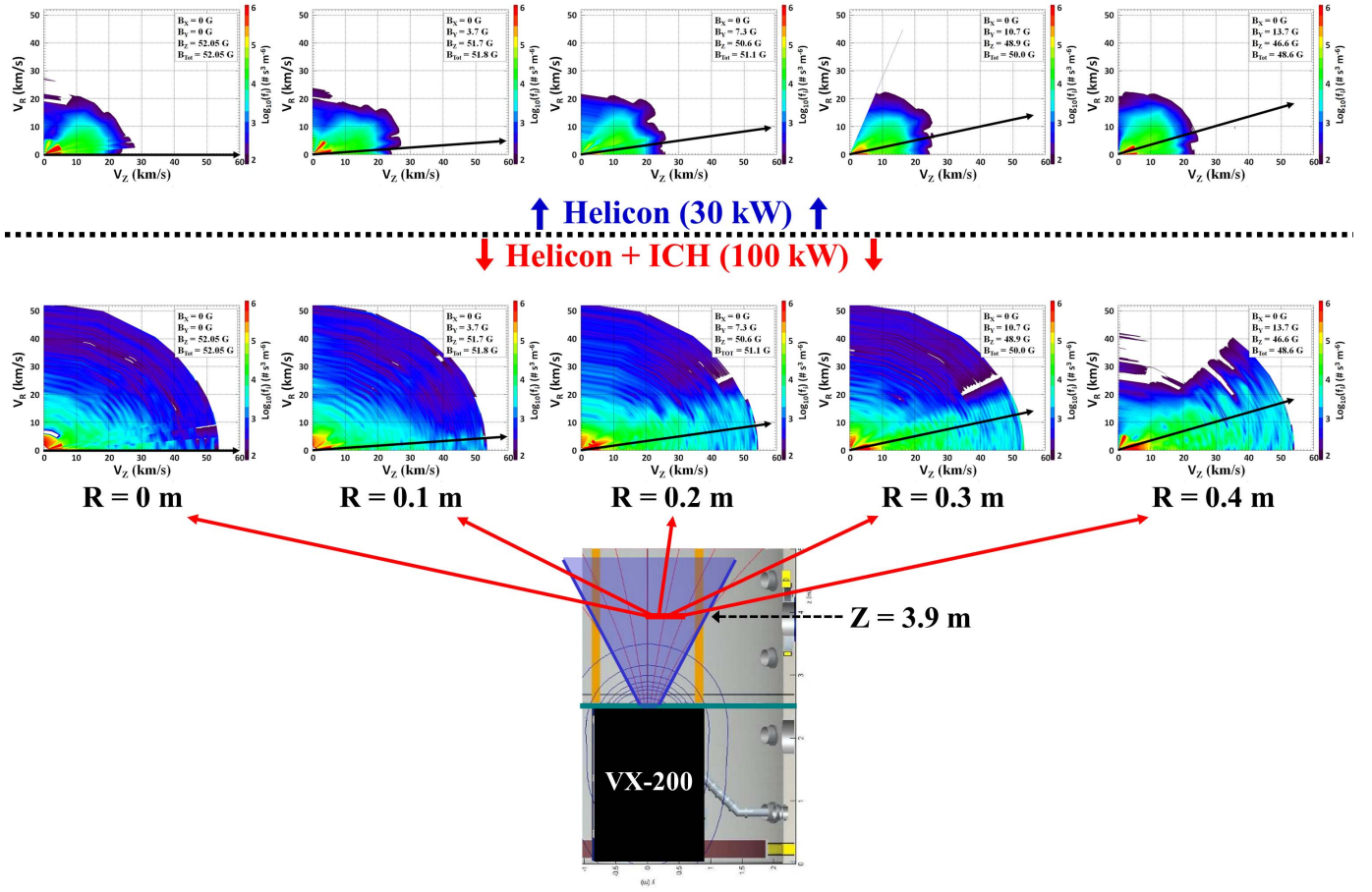


Fig. 10. Contour maps of the ion velocity distribution function as a function of V_R and V_Z arranged according to radial position (columns), helicon (top row), and helicon + ICH (bottom row) operation. The local magnetic field vector is overlain in each plot (black arrow). A diagram illustrating the relative position of the measurements is provided below the contour maps.

ion velocity are shown in Fig. 10. The local magnetic field vector is shown in each plot along with the magnitudes of each component as an inset.

Much of the plume behavior exhibited in the previous data can be seen in these pitch angle distributions. For example, during helicon operation the ions were observed to expand faster radially than the magnetic field and signatures of this are seen as a broadened angular distribution with increasing radial position. During helicon + ICH operation the ions remain fairly well directed ($\theta < 45^\circ$) regardless of radial position suggesting convergent flow. In either case, the ions do not show any signs of predominant magnetization especially at the larger radial distances where the field has begun to curve away. If the ions were magnetized much of the distribution would be expected to be more preferentially organized near the angle of the magnetic field vector. This effect is not observed and the ion flow appears to ignore the influences of the magnetic field. This combined behavior of the ions offers a secondary confirmation that the ions are effectively detached from the magnetic nozzle at this point in the plume.

2) *Comparison With Theory*: Given the above data presents evidence of ion flux separating from its own magnetic flux surfaces, is this detachment consistent with any of the published theories? One of the leading theories involves MHD

field line stretching [4], [5] where the flow of a single fluid becomes energetic enough to drag the magnetic field lines along with the plume negating the necessity for field line separation. This frozen-in flow theory is inconsistent with the data as it requires large scale changes to the magnetic field structure in the plume. Expected changes in the magnetic field strength using parameters from this experiment typically exceeded 5 G, even near-axis, which are easily resolved with the magnetic instrumentation used. Changes on this order were neither observed ($\Delta B_{z,\max} \sim 0.2$ G) in the axial data (Fig. 6) nor in an expanded version of this paper [1]. This finding appears to contradict the conclusion of a similar previous experiment [36], where the field line stretching detachment mechanism was inferred without presenting any directly measured magnetic field data. The experimental data presented here employ a wider range of plasma diagnostics, a larger measurement region and extended magnetic nozzle, and a more capable plasma source. The experiments agree in that an effectively detached flow of electrons and ions is coincident with the location of the super-Alfvénic transition but differ on the mechanism that effects the separation from the magnetic field [1].

Another theory, serving as a fundamental lower limit to detachment, known as electron inertia [8] where ions and

electrons are electrostatically bound only drifting across the magnetic field lines if certain conditions are met. A governing parameter in this electron inertia theory is a scaling parameter, G , that involves the cyclotron frequencies as well as the plume radius and velocity at the nozzle throat and it is stated that smaller values of G are more favorable for detachment [8]. The scaling parameter values for this experiment are 4.3×10^6 and 1.1×10^6 for plasma during helicon and helicon + ICH, respectively. Accordingly, <1% of the plume should be separating within the premise of this theory, which is not the case (Fig. 9). Electron inertia may find more applicability upon considering additional effects found in essentially all plasmas. Ahedo and Merino [37] have shown this theory to be formally wrong and the data from this paper gives experimental support to that claim.

The theory most consistent with the ion detachment data presented above is a loss of adiabaticity [6], [7], [38]. This theory is essentially one of demagnetization where the ions are unable to change gyro-motion parameters on the same scale as the diverging magnetic field. The diverging nozzle field enables perpendicular to parallel ion velocity vector conversion when the magnetic moment, μ , is conserved. The magnetic moment is conserved so long as the action integral in Faraday's law remains valid and breaks down when the particle gyro-orbit becomes too eccentric. An equation illustrating this magnetic moment breakdown is [6]

$$\frac{\Delta r_{Li}}{r_{Li}} \approx \frac{\Delta \Omega_i}{\Omega_i} = \frac{v_i}{f_{ci}} \frac{|\nabla B|}{B}. \quad (6)$$

This states that the magnetic moment will no longer be conserved when the change in Larmor radius becomes comparable with itself, or when the ratio of the Larmor radius to magnetic field scale length ($L_B \sim B/|\nabla B|$) is of order unity. Along the region where the lines of constant ion flux begin to diverge from the magnetic flux in Fig. 9, the right hand side of (6) has a range of 1.6–4.3 and 2.2–4.9 for the helicon and helicon + ICH phases, respectively. These ranges are both of order unity, are consistent in magnitude across each detachment zone, and show agreement between ion flux probe data with magnetometer/RPA data. Recent simulations have been presented showing ions detaching upon demagnetization and give support to this data [39]. Ion detachment via loss of adiabaticity is entirely plausible if not considered confirmed altogether.

B. Electron Cross-Field Transport

Up to this point most of the focus has been on the dynamics of the ions in the flow. Electrons, unlike the ions, are presumed to still be magnetized as the right hand side of (6) is still a few orders of magnitude below unity (<0.013) over the entire measurement range of this experiment. Therefore, in the scenario that the ions have become demagnetized electrons must find a means of crossing the magnetic field lines, until they also become nonmagnetized, otherwise large scale electric fields may arise as space-charge limits become unbalanced. The latter is not occurring given that the plasma potential data from Fig. 7 show no large transitions indicating only moderate dc electric fields. There is also the possibility that counter-streaming electrons forming localized longitudinal currents

may form mitigating these effects, but key signatures of these currents were looked for but not seen [1]. This conclusion only leaves the possibility that magnetized electrons will either cause drag forces to arise on the ions, be impelled to cross the field lines in the wake of the ions, or both to some degree. In the case of electrons crossing the field lines in pursuit of the ions, it must be required that they do so at approximately the same velocity as the ions to preserve quasi-neutrality. It is then necessary to look for signatures of cross-field electron transport across the measurement region.

1) *Coulomb Collisions:* One of the more straight forward mechanisms for electrons to cross magnetic field lines is through collisions. Estimation of the classical collision frequency was done using the test particle model for electrons and singly charged ions [40]

$$v_{\alpha\beta}(V) = \frac{n_\beta q^4 \ln \Lambda}{2\pi \epsilon_0^2 m_\alpha^2 V^3} [\phi(a_\beta V) - \psi(a_\beta V)] \quad (7)$$

$$a_\beta = \sqrt{\frac{m_\beta}{2k_B T_\beta}} \quad (8)$$

where the subscripts α and β refer to the test particle and field particles, respectively, V is the test particle velocity, $\ln \Lambda$ is the Coulomb logarithm, $\phi(x)$ is the error function, and $\psi(x)$ is the derivative of $\phi(x)$. Equation (7) may be simplified using limiting or asymptotic values for $\phi(x)$ and $\psi(x)$, a valid assumption in this case, and in the form of Trubnikov [41] collision frequencies perpendicular and parallel to the magnetic field may be computed. Estimated collision frequencies and inverse Hall parameters (v_c/Ω_c) taken along the nozzle axis are shown in Fig. 11. Collisions with neutrals are shown for reference and were computed using the NRL formulary [40]. The test particles are depicted by symbols (o for electrons, + for ions) and the scattering particles are indicated by line color (blue for electrons, red for ions, and black for neutrals).

These data show that there are large differences in terms of collision frequency between the electrons and ions. Collisions from the ions as well as collisions upon neutrals can essentially be ignored. The electron collision frequency and its role in diffusion must be considered in the transport analysis. The inverse Hall parameter, which is a measure of the number of collisions per gyro-orbit, data shows that despite being able to complete several gyrations about the magnetic field lines before a collision occurs that net transport of the electrons is possible.

2) *Cross-Field Diffusion:* The collision estimates above show that while electron collisions may not be ignored, the question is then whether the rate of cross-field transport is sufficient to match the outflow rate of the ions (~ 13 – 17 km/s during helicon and ~ 27 – 31 km/s with the addition of ICH). Net cross-field transport requires that the colliding particle undergoes a $\pi/2$ deflection. Since electron→electron collisions, despite having a collision frequency near electron→ion collisions, have an equal probability of inward versus outward deflection and cannot account for net transport. It is common practice to therefore ignore electron→electron collisions as a net transport mechanism. Electron→ion collisions, due to

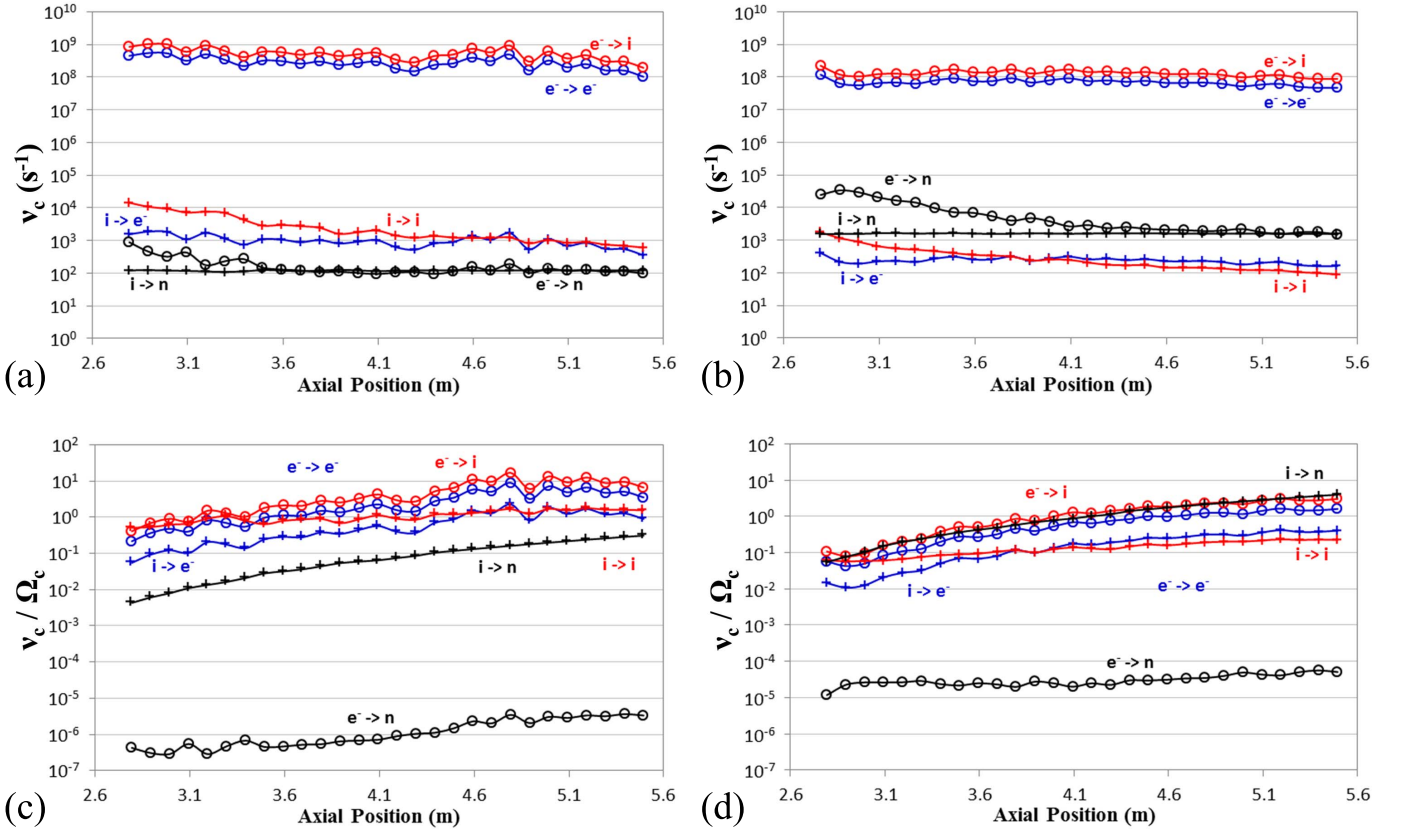


Fig. 11. Collision frequency and inverse Hall parameter data along the nozzle axis during (a) and (c) helicon and (b) and (d) helicon + ICH operation. Test particles are represented by symbols (o electron, + ion) while line color indicates the scatterer (blue—electrons, red—ions, and black—neutrals).

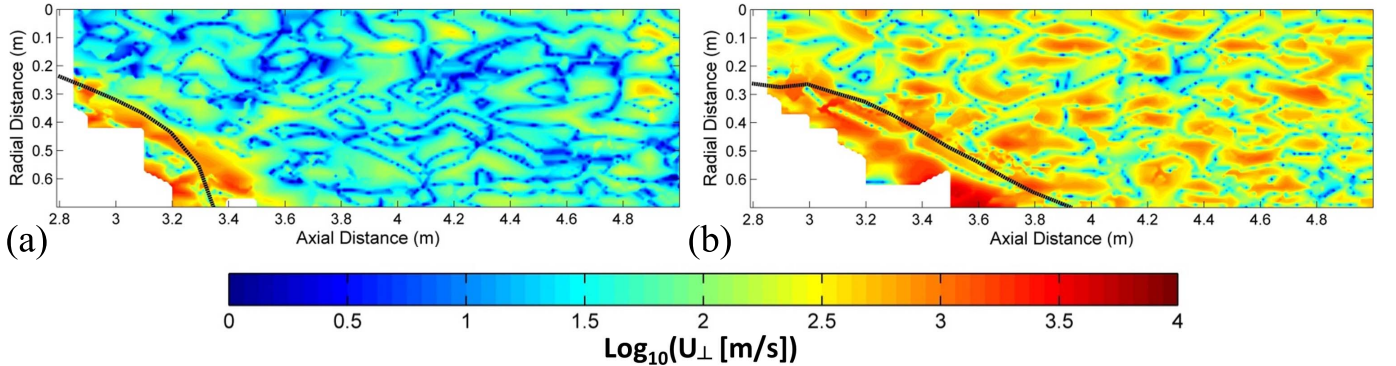


Fig. 12. Net cross-field diffusion due to electron→ion collisions during (a) helicon and (b) helicon + ICH operation. An effective plume edge (black), taken from the ion flux line $f_i = 0.9$, is overlain for reference.

the mass difference, deflect the electrons while the ions are relatively unaffected and can thus lead to net electron transport. To estimate the cross-field velocity due to electron→ion collisions, the equations governing this process, derived from Fick's law, are [42]–[44]

$$u_{e\perp} = -\mu_{\perp} E_{\perp} - D_{\perp} \frac{\nabla n_{\perp}}{n} \quad (9)$$

$$D_{\perp} = \frac{k_B T_e}{m_e \nu_{ei}} \frac{1}{1 + \left(\frac{\Omega_e}{\nu_{ei}}\right)^2}. \quad (10)$$

Equation (9) is a generalized cross-field electron velocity that contains contributions from particle mobility

($\mu_{\perp} = q D_{\perp} / k_B T_e$) reacting to an electric field and diffusion across a density gradient (10). The dc electric field is taken from the negative gradient of the plasma potential using data from the guard-ring Langmuir probe and the component perpendicular to the magnetic field is computed using the angle between the electric field and magnetic field vectors. The diffusion coefficient (including collision parameters) and density gradient are computed using data taken from the guard-ring probe, RPA, and magnetometer. The sign, and thus radially inward or outward transport, is determined by the direction of the gradient of the plasma potential and density as well as the type of charge. One would expect in this plume that the diffusion term would impel both ions and electrons radially

outward, while the mobility term would move the electrons inward and the ions outward. In the case of electron transport, the question is then which contribution is more dominant having the greater magnitude?

The net perpendicular cross-field velocity of electrons due to electron→ion collisions has been computed using mapped quantities and is shown in Fig. 12. Although the figures appear noisy, common as taking gradients accentuates noise in data, valuable trends still emerge. The largest cross-field velocities are seen along the plume edges (outside the black lines) where the density gradient is largest and the diffusion contribution dominates. Inside of the plume ($< f_i = 0.9$) it is found that the mobility contribution, enabling inward transport of electrons, is greater due to dc electric fields within the plasma. Outside of the plume ($> f_i = 0.9$) the density gradient largely dominates causing radially outward transport of electrons. A map of each computed contribution to the net electron transport is presented in a separate work [1]. Nonetheless, electron→ion collisions cannot alone account for the velocities needed to match the ions as they are insufficient by at least an order of magnitude. Additional processes must be occurring to facilitate the detachment process.

3) *Anomalous Transport*: Anomalous resistivity has been mentioned as a possible mechanism to enhance cross-field particle transport in the detachment process [8], [9], [18], [45]. It is described as a means to increase the effective collision rate above interparticle collisions, up to the Bohm limit ($D_{\text{Bohm}} = T/B$), through interactions between particles and a high frequency wave (e.g., oscillating electric field). The waves are introduced through turbulence as the plasma responds to perturbing instabilities. The modified two-stream instability has been mentioned as viable candidate [33] in curved magnetic fields as the ions and magnetized electrons drift apart, with particular interest in frequencies near the lower hybrid where both particles responses are maximized [i.e., lower hybrid drift instability (LHDI)]. As a result of these instabilities it has been found that the fluctuations in density and electric field are in phase [45] and creates an effective resistivity above the collisional value [33]

$$\eta_{\text{eff}} = \eta_c + \eta_{\text{AN}} \approx \eta_c + \frac{\langle \tilde{n}_e \tilde{E} \rangle}{qu_{de} \langle \tilde{n}_e \rangle^2} \quad (11)$$

where the tilde denotes fluctuating quantities, $\langle \rangle$ represents the time average of enclosed parameters, and u_{de} is drift velocity of the electron beam relative to the ion beam. The contribution from anomalous resistivity (η_{AN}) would normally include oscillating magnetic field components [46], but are presumed negligible compared with the electric field. It is left as future work to measure the high-frequency components of the magnetic field and its role in anomalous transport. The effective resistivity modifies the perpendicular diffusion coefficient (and likewise electron mobility) to [47]

$$D_{\perp} = \frac{k_B T_e}{qB} \left(\frac{\Omega_e \tau_{\text{eff}}}{1 + (\Omega_e \tau_{\text{eff}})^2} \right) \quad (12)$$

$$\tau_{\text{eff}} = \frac{m_e}{\eta_{\text{eff}} q^2 n_e}. \quad (13)$$

The effective momentum transfer time, τ_{eff} , is the time interval for momentum exchanges between the electrons and

fluctuating electric field and is the inverse of the effective collision frequency.

If anomalous transport were to be applicable in this setup, signatures of a high-frequency electric field, particularly near the lower hybrid frequency, should arise throughout the regions of the nozzle where ions have deviated from the magnetic field. The high-frequency electric field probe was used to explore these effects. Due to the orientation of the probes' electrodes, only the radial component of the electric field (E_r) was measured searching frequencies up to 10 MHz. Recalling that the probe was located ~ 33 -cm downstream the other diagnostics, due to material thermal limitations, the regions indicating ion separation were unable to be measured. Nevertheless studying high-frequency phenomena in the expanding, transition, and ballistic regions as parsed by the ion flux data is valuable. Spectra have been taken and mapped out as a function of radial position at discreet axial locations for both phases of VX-200 operation and are shown in Fig. 13. Each contour plot is comprised of the logarithmic value of the radial electric field as a function of frequency and radius and arranged by increasing Z position from bottom to top. A thin black line marks the lower hybrid frequency (f_{LH}) as a function of radial position.

There appears to be an overall trend of increasing radial electric field strength at higher frequencies, likely building to a resonance, both in and out of the plasma flow. It is yet to be determined if this effect is dependent upon the probe/electronics or perhaps a result of the chamber/tuning cavity environment, which is beyond the scope of this paper. Despite this behavior any local variations in the radial electric field should be apparent as the majority of the peaks in this trend to resonance are below 90 V/m for frequencies up to 9.5 MHz, which is far below the electric field magnitudes expected to enable anomalous transport.

Unique to the case of hotter ions (during helicon + ICH) is a distinct structure or grouping of electric field peaks that forms near the edge of the flow coincident with regions of lower magnetic field radial curvature. This observation is significant since the lower curvature may provide a greater divergence of the electrons from the detached ions allowing the instability to form. The greatest amplitude E_r along the edge of the flow was 740 V/m at a frequency of 5.51 MHz, which is approximately $\sim 3f_{\text{LH}}$ suggesting the LHDI may be involved. This edge structure spreads out and dissipates with increasing axial distance before disappearing altogether beyond $Z > 3.93$ m. The locations where this E_r structure spreads to the interior of the plume line up well with the ion flux transition region where the flow linearizes between $3.5 \text{ m} < Z < 3.9 \text{ m}$ in Fig. 9. The vanishing of the structure altogether in the weaker magnetic field correlates well with the ion flux ballistic/linear region $Z > 3.9 \text{ m}$ in Fig. 9, indicating the instability is no longer active, electron/ion separation has minimized, and the flow has effectively detached from the magnetic nozzle. The structure is not readily observed during phases of operating the helicon source alone, which either does not exist or was not measured far enough radially. It is left as future work to explore electric and magnetic field phenomena at higher frequencies, at greater radii, and along multiple vector components.

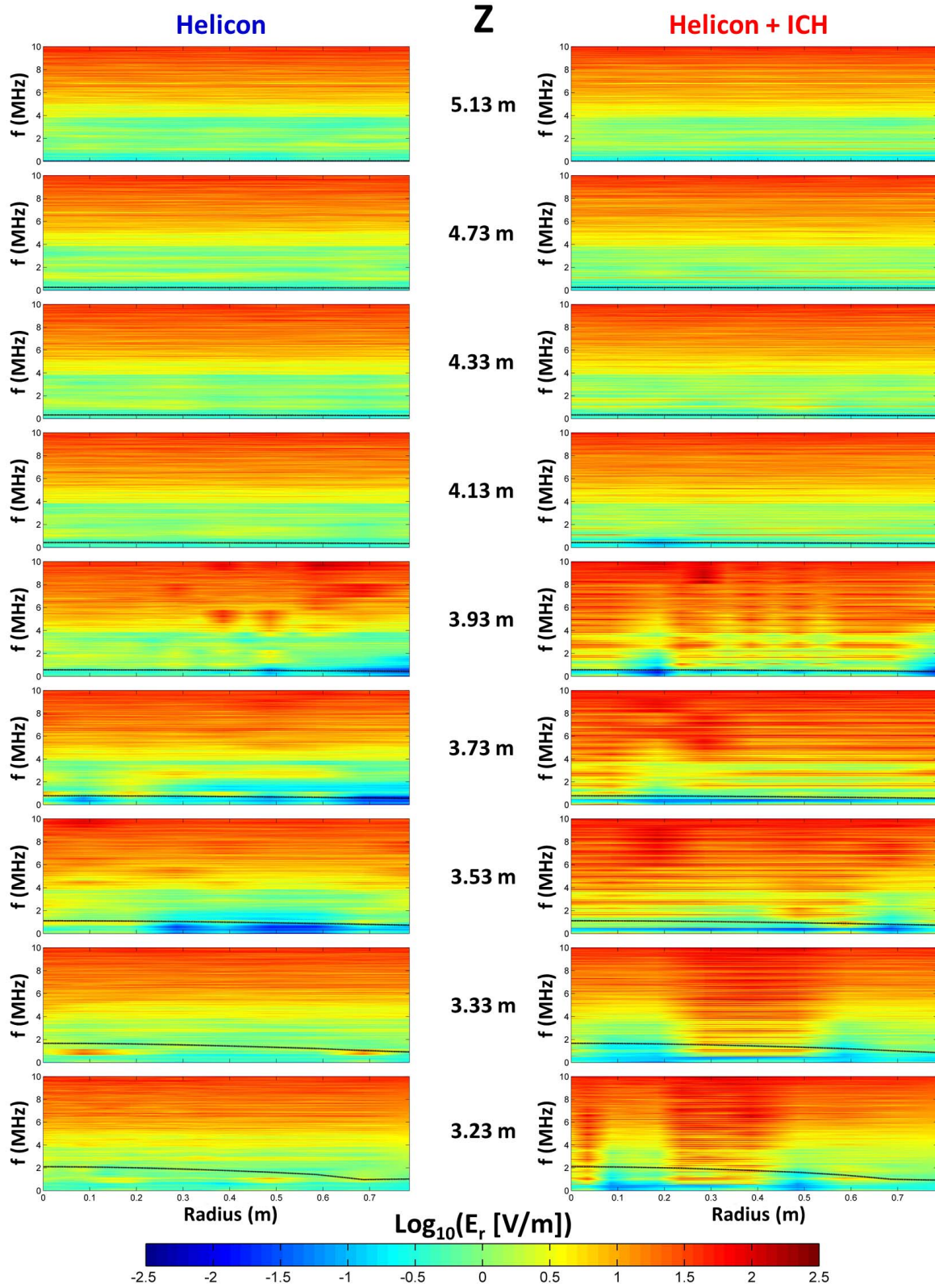


Fig. 13. Composition of radial electric field strength contours as a function of frequency and radius for both helicon (left) and helicon + ICH (right) operation. The contours are arranged by axial location of the scan (rows, increasing bottom to top). The lower hybrid frequency as a function of radius is plotted for reference (black line).

4) *Force Balance*: It has just been shown that a strong high-frequency electric field develops along the edges of the plume. Does this mean that anomalous cross-field transport

of electrons is a certainty? Not necessarily, especially in the regions of the nozzle where the magnetic field is prohibitive, but it is one of the possible outcomes. As indicated earlier in

this section, the behavior of the flow will ultimately depend upon an electrostatic force balance between the ions and electrons and how each respond to the fluctuating electric fields in the plume. The ion response to these fluctuating fields will be to follow electrons along the magnetic field lines where the electric fields are large enough to balance or exceed the centrifugal force on the ions, thus trapping them in the magnetic field

$$E_{\perp \text{Ion Trapping}} = \frac{m_i v_i^2}{q R_c} \quad (14)$$

where R_c is the radius of curvature of the interacting magnetic field line. The electron response is to diffuse anomalously across the outer magnetic field lines to follow the ballistic ions along more centrally located field lines. The enabling electric field in this scenario is then the ratio of the cross-field electron velocity to the anomalous mobility

$$E_{\perp \text{Anomalous}} = \frac{u_{\perp}}{\mu_{\perp}} = v_i \sin \theta B \left(\frac{1 + (\Omega_e \tau_{\text{eff}})^2}{\Omega_e \tau_{\text{eff}}} \right). \quad (15)$$

The cross-field electron velocity (u_{\perp}) required to abate space-charge buildup due to ions departing with velocity, v_i , is the product of the ion velocity and the sine of the separation angle of the ions and magnetic field line.

The balance of forces, an electrostatic tug-of-war, to determine which process dominates between ion trapping and anomalous resistivity depends upon the localized microscale conditions in the plume. The process requiring the lower electric field strength will saturate and never reach the field strength necessary for the other process to operate. It should then be expected that the ion trapping process will dominate ($\langle \tilde{E}_{\perp} \rangle_{\text{Ion Trapping}} < \langle \tilde{E}_{\perp} \rangle_{\text{Anomalous}}$) in high-magnetic field regions, areas where the radius of curvature is large, and/or for lower ion mass and velocity. Conditions for anomalous resistivity to dominate ($\langle \tilde{E}_{\perp} \rangle_{\text{Anomalous}} < \langle \tilde{E}_{\perp} \rangle_{\text{Ion Trapping}}$) would then be for heavier or faster ions, lower magnetic fields, larger effective collision frequency, and/or lower radius of curvature.

Based on the measured data and an assumed range of $1 < \Omega_e \tau_{\text{eff}} < 16$, the theoretical minimum to experimental equivalent Bohm diffusion [47], conditions are permissible for both of these processes to exist in different regions of the plume [1]. The electric fields required to maintain curvature motion and trap the ions are lower in more upstream regions ($Z < 3.4$ m). Assuming low divergence angles and greater mobility ($\Omega_e \tau_{\text{eff}} < 6$), anomalous transport would be the more effective process for axial ranges $Z > 3.5$ m. The region between $3.4 \text{ m} < Z < 3.5 \text{ m}$ would then be a thin zone transitioning between the two processes and are shown in Fig. 14. These computed regions are consistent with the trends observed in the integrated ion flux data [Fig. 9(b)]. After deviating from the magnetic field the ions flare out radially between $2.9 \text{ m} < Z < 3.5 \text{ m}$ during helicon + ICH, coincident with the ion trapping region. Inflection points in the lines of constant ion flux mark the zone transitioning to ballistic flow between $3.4 \text{ m} < Z < 3.9 \text{ m}$ and are coincident with the estimated anomalous transport region. Beyond

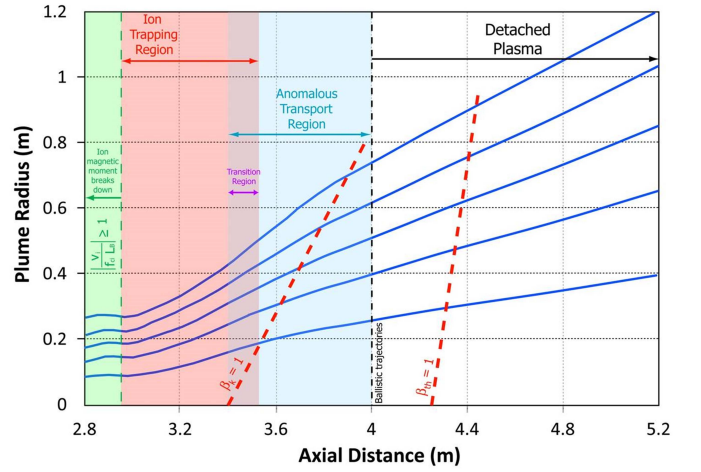


Fig. 14. Image summarizing the various regions associated with the detachment process from a magnetic nozzle during helicon + ICH operation. The flow lines (blue) are based on the integrated ion flux and extended out along the linear region. Lines showing the transition above unity for kinetic and thermal beta are displayed for reference (red dashed).

$Z > 4.0$ m the trajectories are linear and the fluctuating electric fields have dissipated indicating that the flow, as a whole, is effectively detached for practical purposes, from the magnetic nozzle. The electrons are still magnetized, but move with the ions in the weaker magnetic field regions until adiabaticity is presumably lost further downstream. Shown for reference are lines of demarcation for the super-Alfvénic flow transition ($\beta_k = n_i m_i v_i^2 / B^2 / \mu_0 = 1$) and thermal beta ($\beta_{th} = n_i k_B T_i / B^2 / 2 \mu_0 = 1$) transition. Curious is that the super-Alfvénic transition covers the span of the anomalous transport region without any significant changes to the magnetic field structure of the applied field as anticipated by MHD detachment theories [4], [5]. The plasma flow is energetically capable of stretching the magnetic field lines, if considered as a single fluid, but if taken as two fluids or even as individual particles the ions could then be considered energetically capable of pulling electrons across the field.

The magnitude of the fluctuating electric field in both the ion trapping and anomalous transport region is sufficient to carry out each process for several of the frequencies where spectral peaks are located. These field strengths can be used to estimate an approximate anomalous transport rate necessary to carry out these observations. Using electric field (at 5.51 MHz), magnetic field, and ion velocity data along the anomalous transport region ($3.5 \text{ m} < Z < 4.0 \text{ m}$) at a divergence angle of 10° , the transport parameter is approximately $\Omega_e \tau_{\text{eff}} \sim 4.0$. This value is closer to the Super-Bohm values ($\Omega_e \tau_{\text{eff}} \sim 2.7$) reported in [47] than it is for the commonly accepted, experiment dependent, Bohm value of 16. This estimated transport parameter equates to an effective collision rate of $\sim 3.5 \times 10^8 \text{ s}^{-1}$, which is a factor of 4 ± 1 above the electron→ion collision frequency. This higher effective collision frequency, in addition to the effects of the oscillating electric field on the classical mobility, would bring the electron cross-field velocity within a factor of two for the required values to match the detached ion velocity [1].

These processes and rates are reported for the more energetic plasma flows during helicon + ICH operation. It appears

that ion trapping or radial ambipolar forces dominate the plume behavior for lower ion velocity flow during helicon only operation. Although not directly observed, anomalous transport may still be occurring in the weak magnetic field regions beyond the limits of the translation stage. It may be the focus of future experiments to explore the plume further out in radius during plasma operation at lower ion energy.

IV. CONCLUSION

An experiment using the VASIMR VX-200 device operating at a power level of 100 kW was carried out to map the behavior of plasma flowing through a magnetic nozzle and to study the detachment process. The plasma was not following the applied magnetic field, indicated by data from multiple plasma diagnostics. Key indications of detached flow were from mapped lines of constant integrated ions flux, an RPA pitch angle distribution, and a spatially dependent high frequency electric field. Plasma detachment is best described as a two part process first involving the separation of the ion from the magnetic field through the breakdown of the ion magnetic moment. The second part involves turbulence, created by instabilities, where a fluctuating electric field facilitates competing interactions between detached ion and magnetized electrons. In stronger magnetic field regions the electrons are more tightly bound to the field and the ion are temporarily trapped flaring outward as the field expands. As the magnetic field weakens the ion begin to dominate and the electrons respond to the turbulent electric field through enhanced anomalous transport. The electrons cross the magnetic field lines pursuing the ion until the turbulent electric field dissipates and the ion trajectories linearize resulting in an effectively detached plume ~ 2 -m downstream of the nozzle throat.

Future work may include making the same measurements out to greater radii, including new hardware to measure the axial component of the high frequency electric field, and explore for effects from a plausible high frequency magnetic field to better characterize anomalous transport rates in the plume. Also possible may be to explore the detachment processes at various VASIMR power levels (i.e., multiple ion energies), propellant flow rates, and propellant species.

REFERENCES

- [1] C. S. Olsen, "Experimental characterization of plasma detachment from magnetic nozzles," Dept. Phys. Astronomy, Rice Univ., Houston, TX, USA, Tech. Rep. 1911/72016, 2013, p. 298.
- [2] E. Ahedo, "Plasmas for space propulsion," *Plasma Phys. Controlled Fusion*, vol. 53, no. 12, p. 124037, 2011.
- [3] R. A. Gerwin *et al.*, "Characterization of plasma flow through magnetic nozzles," Los Alamos National Laboratory, Los Alamos, NM, USA, Tech. Rep. ADA221044, 1990, p. 173.
- [4] A. V. Arefiev and B. N. Breizman, "Magnetohydrodynamic scenario of plasma detachment in a magnetic nozzle," *Phys. Plasmas*, vol. 12, no. 4, pp. 043504-1–043504-10, 2005.
- [5] B. N. Breizman, M. R. Tushentsov, and A. V. Arefiev, "Magnetic nozzle and plasma detachment model for a steady-state flow," *Phys. Plasmas*, vol. 15, no. 5, pp. 057103-1–057103-10, 2008.
- [6] M. D. Carter *et al.*, "Radio frequency plasma applications for space propulsion," in *Proc. Int. Conf. Electromagn. Adv. Appl.*, Turin, Italy, 1999.
- [7] K. Terasaka, S. Yoshimura, K. Ogiwara, M. Aramaki, and M. Y. Tanaka, "Experimental studies on ion acceleration and stream line detachment in a diverging magnetic field," *Phys. Plasmas*, vol. 17, no. 7, pp. 072106-1–072106-6, 2010.
- [8] E. B. Hooper, "Plasma detachment from a magnetic nozzle," *J. Propuls. Power*, vol. 9, no. 5, pp. 757–763, 1993.
- [9] E. Ahedo and M. Merino, "On plasma detachment in propulsive magnetic nozzles," *Phys. Plasmas*, vol. 18, no. 5, pp. 053504-1–053504-8, 2011.
- [10] E. Bering, B. Longmier, T. Glover, F. C. Diaz, J. Squire, and M. Bruckard, "High power electric propulsion using VASIMR: Results from flight prototypes," in *Proc. 47th AIAA Aerosp. Sci. Meeting and Exhibit*, Orlando, FL, USA, 2009.
- [11] B. W. Longmier *et al.*, "Improved efficiency and throttling range of the VX-200 magnetoplasma thruster," *J. Propuls. Power*, vol. 30, no. 1, pp. 123–132, 2014.
- [12] F. F. Chen and R. W. Boswell, "Helicons—The past decade," *IEEE Trans. Plasma Sci.*, vol. 25, no. 6, pp. 1245–1257, Dec. 1997.
- [13] R. W. Boswell and F. F. Chen, "Helicons—The early years," *IEEE Trans. Plasma Sci.*, vol. 25, no. 6, pp. 1229–1244, Dec. 1997.
- [14] J. P. Squire *et al.*, "VASIMR performance measurements at powers exceeding 50 kW and lunar robotic mission applications," in *Proc. Int. Interdiscipl. Symp. Gaseous and Liquid Plasmas*, Sendai, Japan, 2008.
- [15] L. D. Cassady *et al.*, "VASIMR technological advances and first stage performance results," in *Proc. 45th AIAA/ASME/SAE/ASEE Joint Propuls. Conf. Exhibit*, 2009.
- [16] B. W. Longmier *et al.*, "VASIMR VX-200 performance measurements and helicon throttle tables using argon and krypton," in *Proc. 32nd IEPC*, 2011.
- [17] B. W. Longmier *et al.*, "VASIMR VX-200 improved throttling range," in *Proc. 48th AIAA/ASME/SAE/ASEE Joint Propuls. Conf.*, 2012.
- [18] A. V. Arefiev and B. N. Breizman, "Theoretical components of the VASIMR plasma propulsion concept," *Phys. Plasmas*, vol. 11, no. 5, pp. 2942–2949, 2004.
- [19] E. A. Bering *et al.*, "Observations of single-pass ion cyclotron heating in a trans-sonic flowing plasma," *Phys. Plasmas*, vol. 17, no. 4, pp. 043509-1–043509-19, 2010.
- [20] T. H. Stix, "Ion cyclotron heating of a plasma," *J. Nucl. Energy C, Plasma Phys., Accelerators, Thermonucl. Res.*, vol. 2, no. 1, p. 84, 1961.
- [21] J. P. Squire *et al.*, "Superconducting 200 kW VASIMR experiment and integrated testing," in *Proc. 31st Int. Electric Propuls. Conf.*, 2009.
- [22] W. Lochte-Holtgreven, "Plasma diagnostics," in *American Vacuum Society Classics*, 2nd ed. New York, NY, USA: AIP Press, 1995, p. 928.
- [23] B. W. Longmier *et al.*, "Ambipolar ion acceleration in an expanding magnetic nozzle," *Plasma Sources Sci. Technol.*, vol. 20, no. 1, p. 015007, 2011.
- [24] C. S. Olsen, "Ion flux maps and helicon source efficiency in the VASIMR VX-100 experiment using a moving langmuir probe array," in *Physics and Astronomy*. Houston, TX, USA: Rice Univ. Press, 2009, p. 155.
- [25] D. G. Chavers and F. R. Chang-Díaz, "Momentum flux measuring instrument for neutral and charged particle flows," *Rev. Sci. Instrum.*, vol. 73, no. 10, pp. 3500–3507, 2002.
- [26] X. Chen, "The impact force acting on a flat plate exposed normally to a rarefied plasma plume issuing from an annular or circular nozzle," *J. Phys. D, Appl. Phys.*, vol. 43, no. 31, p. 315205, 2010.
- [27] D. G. Chavers, F. R. Chang-Díaz, C. Irvine, and J. P. Squire, "Momentum and heat flux measurements in the exhaust of VASIMR using helium propellant," in *Proc. 28th Int. Electr. Propuls. Conf.*, 2003.
- [28] B. W. Longmier *et al.*, "Validating a plasma momentum flux sensor to an inverted pendulum thrust stand," *J. Propuls. Power*, vol. 25, no. 3, pp. 746–752, 2009.
- [29] L. W. Parker, "Theory of a satellite electrostatic probe," *Ann. Phys.*, vol. 44, no. 1, pp. 126–161, 1967.
- [30] E. A. Bering, K. G. Weber, and U. V. Fahleson, "An upper limit on the aperture separation of ion drift meters," *Astrophys. Space Sci.*, vol. 83, nos. 1–2, pp. 37–49, 1982.
- [31] E. A. Bering, III, F. Chang-Díaz, and J. Squire, "The use of RF waves in space propulsion systems," 2004.
- [32] T. Hurtig and J. Wistedt, "Probes for high-frequency measurements in a plasma gun," *Rev. Sci. Instrum.*, vol. 74, no. 2, pp. 1153–1155, 2003.
- [33] T. Hurtig, N. Brenning, and M. A. Raadu, "The role of high frequency oscillations in the penetration of plasma clouds across magnetic boundaries," *Phys. Plasmas*, vol. 12, no. 1, pp. 012308-1–012308-13, 2005.
- [34] J. S. Bendat and A. G. Piersol, "Random data analysis and measurement procedures," *Meas. Sci. Technol.*, vol. 11, no. 12, p. 1825, 2000.
- [35] J. P. Squire *et al.*, "VASIMR VX-200 operation at 200 kW and plume measurements: Future plasma and an ISS EP test platform," in *Proc. 32nd IEPC*, 2011.
- [36] C. A. Deline *et al.*, "Plume detachment from a magnetic nozzle," *Phys. Plasmas*, vol. 16, no. 3, pp. 033502-1–033502-9, 2009.

- [37] E. Ahedo and M. Merino, "Two-dimensional plasma expansion in a magnetic nozzle: Separation due to electron inertia," *Phys. Plasmas*, vol. 19, no. 8, pp. 083501-1–083501-9, 2012.
- [38] K. Terasaka, S. Yoshimura, K. Ogiwara, M. Aramaki, and M. Y. Tanaka, "Observation of ion stream line detachment and onset of azimuthal rotation in a diverging magnetic field," *IEEE Trans. Plasma Sci.*, vol. 39, no. 11, pp. 2470–2471, Nov. 2011.
- [39] M. Merino and E. Ahedo, "Magnetic nozzle far-field simulation," in *Proc. 48th AIAA/ASME/SAE/ASEE Joint Propuls. Conf. Exhibit.*, 2012.
- [40] J. D. Huba, *NRL Plasma Formulary*. Washington, DC, USA: The Office of Naval Research, 2012.
- [41] B. A. Trubnikov, "Particle interactions in a fully ionized plasma," in *Reviews of Plasma Physics*, vol. 1. New York, NY, USA: Consultants Bureau, 1965, p. 105.
- [42] M. A. Lieberman and A. J. Lichtenberg, *Principles of Plasma Discharges and Materials Processing*, 2nd ed. Hoboken, NJ, USA: Wiley, 2005, p. 757.
- [43] F. F. Chen, "Introduction to plasma physics and controlled fusion," in *Plasma Physics*, vol. 1, 2nd ed. New York, NY, USA: Plenum Press, 1984, p. 421.
- [44] D. M. Goebel and I. Katz, "Basic plasma physics," in *Fundamentals of Electric Propulsion*. New York, NY, USA: Wiley, 2008, pp. 37–90.
- [45] N. Brenning, T. Hurtig, and M. A. Raadu, "Conditions for plasmoid penetration across abrupt magnetic barriers," *Phys. Plasmas*, vol. 12, no. 1, pp. 012309-1–012309-10, 2005.
- [46] E. Y. Choueiri, "Anomalous resistivity and heating in current-driven plasma thrusters," *Phys. Plasmas*, vol. 6, no. 5, pp. 2290–2306, 1999.
- [47] N. Brenning, R. L. Merlino, D. Lundin, M. A. Raadu, and U. Helmersson, "Faster-than-Bohm Cross- B electron transport in strongly pulsed plasmas," *Phys. Rev. Lett.*, vol. 103, no. 22, pp. 225003-1–225003-4, 2009.

Authors' photographs and biographies not available at the time of publication.